ACS Catalysis

pubs.acs.org/acscatalysis Research Article

Self-Sustainable Lattice Strains of Morphology-Tuned Nanowires in Electrocatalysis

Zhijie Kong, Zhi-Peng Wu, Yazan Maswadeh, Gang Yu, Jorge A. Vargas, Dominic Caracciolo, Valeri Petkov, Shuang-Quan Zang,* Li Tao,* Shuangyin Wang,* and Chuan-Jian Zhong*

Cite This: ACS Catal. 2024, 14, 4709−4718 Read Online

ACCESS | Metrics & More | Article Recommendations | Supporting Information

ABSTRACT: The lattice structure is known to influence interfacial reactivities of nanoscale alloy catalysts, but little is known about how the lattice strain can be sustainably controlled by the nanoscale morphology under electrocatalytic reaction conditions. Herein, a previously unknown self-regulated stability of lattice strains is demonstrated by engineering highly active platinum−copper alloy nanowires with two distinctive types of morphology. The dendritic alloy nanowires exhibit the best performance for oxygen reduction reaction among the reported platinum−copper alloy catalysts. In comparison with the initial difference of compressive lattice strains between smooth and dendritic nanowires, the strains are shown to be controllable, which coincides with the highly durable electrocatalytic performance throughout the duration of oxygen reduction reaction despite the occurrence of dealloying. By thorough characterizations of the nanowire morphologies, compositions, and lattice strains, the self-regulated stability of lattice strains is revealed to originate from the operation of a combination of morphology-tuned compressive strain and realloying in the dendritic nanowires for the enhanced electrocatalytic activity and durability. These findings have significant implications for the design of high-durability alloy catalysts in heterogeneous catalysis.

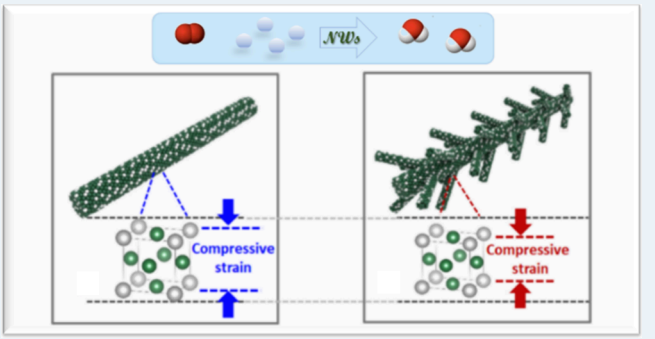

KEYWORDS: *nanowires, platinum−copper alloys, catalysts, electrocatalysts, lattice strains, oxygen reduction reaction, and fuel cells*

1. INTRODUCTION

For metal and alloy nanoparticles with defined phase structures, one of the most important structural parameters is the lattice constant, which differs from those in bulk counterparts. Key to this difference is the lattice strain, which may play a critical role in determining the functional properties of the nanomaterials, especially under operational or reactive conditions where the lattice strain could change as a result of surface or interfacial processes (e.g., dealloying, adsorption). This is exemplified by the catalytic or electrocatalytic performances of transition metal-alloyed platinum nanoparticles,[1−6] where the ability to control the lattice strains in the nanophase structures is essential in terms of activity, selectivity, and durability.[7−10] For example, the as-synthesized Cu_3Pt/C nanoparticles display an ordered intermetallic phase after annealing at 1000 °C, which was shown to yield improved activity and stability upon dealloying.[11] Greeley and Nørskov showed that the dissolution potential of the Pt overlayer on Pt_3M (M = Fe, Co, Ni, Cu, etc.) could be improved by up to 0.16 V in comparison with pure Pt.[12,13] A recent in situ X-ray absorption study of PtCo NPs after dealloying[14] showed a gradual decrease of activity along with a diminished atomic-level strain.[15−17] The compressive strain reduces the formation energy of vacancy, favoring defects, and jagged surface (with defective sites).[18,19] Strasser et al. demonstrated that the selective electrochemical dissolution for as-synthesized alloy leads to lattice mismatch at the interface,[20,21] yielding a compressive strain.[22] Other examples include the observations of a compressive strain for Pt shell on CuPt@Pt core@shell NPs[23] and Pt-based alloy NPs after dealloying.[18,24] The lattice strains are shown to influence significantly the electrocatalytic activity and durability for oxygen reduction reaction. There are also examples demonstrating the significant influences of the lattice strains on the catalytic properties of alloy nanoparticles under different reaction conditions.[25]

Despite the widespread recognition of the significant role of lattice strains of alloy nanoparticles under reactive conditions, little is known about how to control or maintain the lattice strains of the alloy nanoparticles in the electrocatalytic process

Received: January 20, 2024
Revised: February 27, 2024
Accepted: February 28, 2024
Published: March 13, 2024

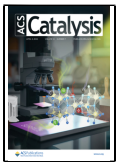

https://doi.org/10.1021/acscatal.4c00451
ACS Catal. 2024, 14, 4709−4718

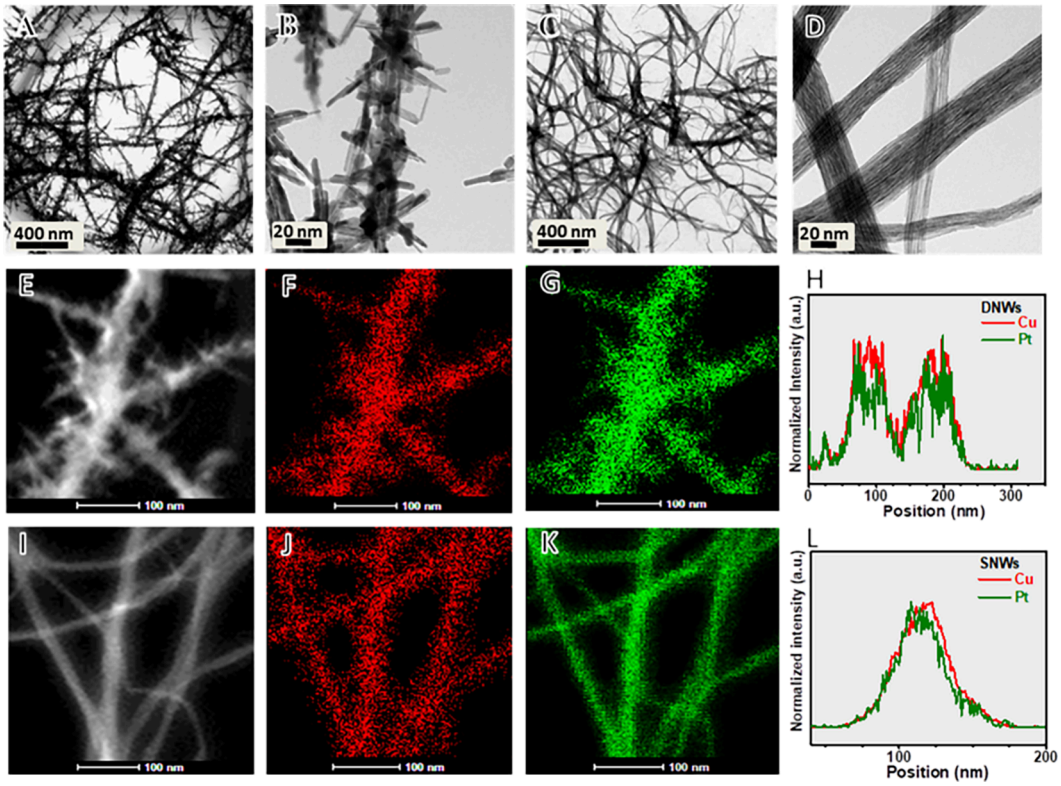

Figure 1. (A, B) TEM images of $Pt_{17}Cu_{83}$ DNWs. (C, D) TEM images of $Pt_{18}Cu_{82}$ SNWs. (E, I) HAADF images. STEM/EDS elemental mapping images for Cu (F, J) and Pt (G, K) of $Pt_{17}Cu_{83}$ DNWs (E–G) and $Pt_{18}Cu_{82}$ SNWs (I–K). The scan line profiles of EDS for $Pt_{17}Cu_{83}$ DNWs (H) and $Pt_{18}Cu_{82}$ SNWs (L), as indicated by the red lines in Figure S5. Green color stands for Pt, red color for Cu. Scale bars: 400 nm (A, C), 20 nm (B, D), and 100 nm (E–G, I–K).

where interfacial or surface reactions occur and often change the lattice strains. We demonstrate here a new strategy to control or maintain the lattice strains in the electrocatalytic processes by exploring the nanowire (NW) morphology self-controlled sustainability of lattice strains. In addition to intriguing optical mechanical, thermal, and sensing properties,[26,27] metal and alloy NWs exhibit geometric flexibility and provide significantly different lattice constants from other shapes mainly due to the elastic relaxation induced by internally mismatched stresses at the edges and sidewalls of NWs. Theoretical and experimental works have shown that the surface strain can induce differences in NW morphology, which could be coupled to a compositional change for an alloyed NW.[28] For example, the percolated regions of lattice contraction are observed for core–shell types of Pt alloy, in contrast to randomly or sporadically distributed contraction or expansion for pure Pt.[29,30] The dislocation center may undergo significant strain changes depending strongly on the morphology and composition of the alloy nanomaterials. Indeed, some of these attributes are explored for Pt-based NWs toward enhancing mass and electron transport[31] in electrocatalytic processes. In the actual electrocatalytic reaction, the lattice strain changes with leaching of the catalyst components. Whether the lattice strain has a sustainable effect on the performance and whether the structure–activity relationship can be significantly reversed in this process still need further discussion. How the precise engineering of the alloy NW morphology could enable the controllable compressive lattice strains toward sustainable electrocatalytic activities remains unknown. To minimize the influence of highly active alkali metal ligands (such as Fe, Co, Ni) on the relationship between activity and lattice strain, Cu was selected as the ligand to form Pt alloys for oxygen reduction reaction.[21] We demonstrated in this report this viability with platinum–copper alloy NWs with two distinctive morphologies, dendritic and smooth NWs. Using the oxygen reduction reaction as a probe reaction condition, a morphology-based self-controllable sustainability of the lattice strains is revealed in correlation with the electrocatalytic activity and durability. The origin of morphology-dependent electrocatalytic activity and durability will be discussed, highlighting the importance of self-controllable morphology compressive lattice strains of the alloy NWs.

2. RESULTS AND DISCUSSION

2.1. Morphologies, Compositions, and Phase Structures. The morphologies of the alloy NWs, $Pt_{17}Cu_{83}$ DNWs (Figure 1A,B), and $Pt_{18}Cu_{82}$ SNWs (Figure 1C,D) are first compared, showing a clear contrast in terms of the surface smoothness and the presence of dendrites. The DNWs show an average diameter around 29 ± 6 nm and branches/tips of 14 ± 5 nm, separately, whereas the SNWs display an average diameter around 20 ± 2 nm, along with a bundle structure of interconnected NWs. Cu DNWs were also synthesized using the Cu^+ precursor (CuCl) (Figure S1). The valence of the Cu precursor and the synthesized time were shown to play an important role in controlling the dendritic and smooth morphologies (Figures S2 and S3). The characterization of the metal distributions of the two types of NWs by HAADF-STEM/DES (Figure 1 and Figure S4) indicates a random distribution of Cu and Pt atoms along and across the NW structure. The results demonstrate the effectiveness of our hydrothermal synthesis method in controlling the alloy NW

https://doi.org/10.1021/acscatal.4c00451
ACS Catal. 2024, 14, 4709–4718

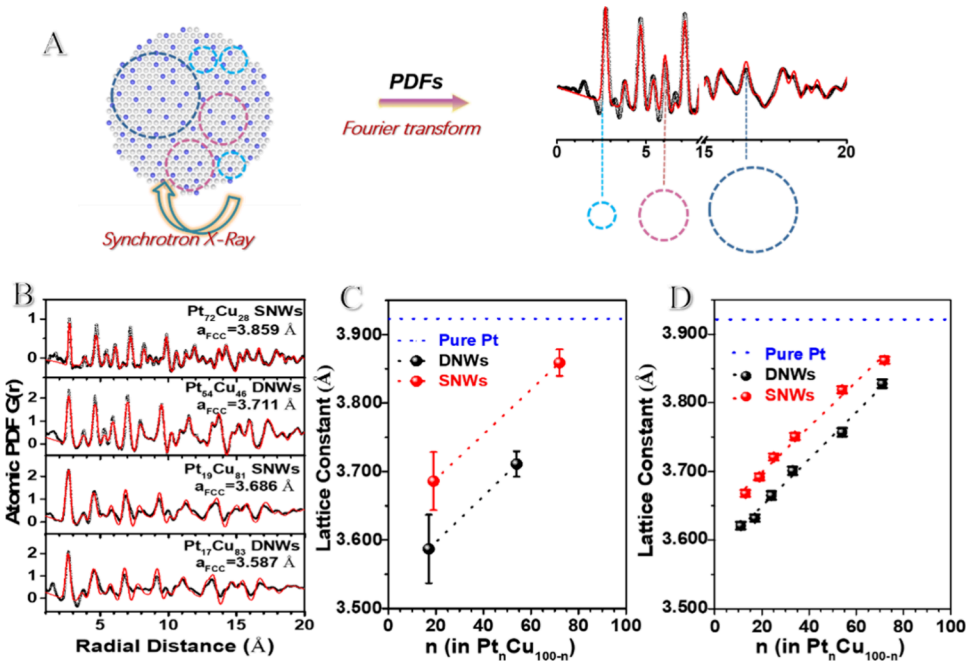

Figure 2. (A) An illustration of atomic PDFs obtained by the synchrotron X-ray data: experiments (black circle) and simulation (red line). Circles with different radius sizes represent different atom pair distance values. (B) Experimental PDF-fit-derived fcc lattice parameters and fcc-model fit to atomic PDFs for PtCu/C DNWs and SNWs of different compositions. The "fcc" lattice parameters were refined by the analysis. (C) Lattice constant vs different composition of Pt_nCu_{100-n}/C DNWs/SNWs based on HE-XRD/PDFs. (D) Lattice constant vs different composition of Pt_nCu_{100-n}/C DNWs/SNWs based on in-house XRD. The dash blue lines indicate the lattice constant for pure Pt nanowires.

morphology and composition. We note that a similar hydrothermal method with a subtle difference in the reaction condition was reported earlier for the synthesis of ultrathin Pt, PtAu, and PtPd NWs and assemblies.[32]

The phase structures of $Pt_{54}Cu_{46}$/C and $Pt_{17}Cu_{83}$/C DNWs as well as $Pt_{72}Cu_{28}$/C and $Pt_{18}Cu_{82}$/C SNWs were characterized by synchrotron HE-XRD, from which experimental pair distribution function (PDF) fit-derived fcc lattice parameters and atomic PDFs (Figure 2A,B) were obtained. The best-fitted data reflect the structure information on fcc-like models with refined fcc-lattice parameters. The fits for binary Pt_nCu_{100-n} NWs with higher Pt components (54 and 72 at. %) outperform those Pt_nCu_{100-n}/C NWs with lower Pt components. A misfit (e.g., in the range of r values from 8 to 10 Å) in the fcc structure with the higher Cu content could be viewed as composed of interpenetrating fcc-like nanodomains, or a lower degree of random distribution with slight nanodomain segregation.[1] In comparison with the higher-Pt-content $Pt_{54}Cu_{46}$/C DNWs, the lower-Pt-content $Pt_{17}Cu_{83}$/C DNWs show an increased percentage of nanophase segregation domains in the alloy structure. The lattice constant (Figure 2C) based on synchrotron X-ray HE-XRD/PDF analysis is in line with that (Figure 2D) obtained from in-house XRD (Figure S5). The lattice constants of DNWs are smaller than those of SNWs at the same composition, which means a higher compressive lattice strain for DNWs. This result demonstrates that the origin of the lattice strain stems from the morphological difference of the two types of NWs, due to the difference in reaction rate of the copper-precursors (Cu(I) and Cu(II)).[33]

In comparison with the SNWs, the Cu $2p_{3/2}$ and Pt $4f_{7/2}$ peak positions of X-ray photoelectron spectroscopy (XPS) for the DNWs slightly decrease and increase, respectively (Figure S6). By a further comparison between XPS and inductive coupled plasma emission spectrometry (ICP) data, a relatively higher Pt enrichment is revealed on the near-surface regions of $Pt_{17}Cu_{83}$/C DNWs than that of $Pt_{18}Cu_{82}$/C SNWs (Figure S7). The binding energy shift is attributed to a change of the coordination environment of surface atoms, and the structural relaxation/shrinking.[9,15,18,34] In comparison with SNWs, there is an increase in the Pt 4f binding energy for DNWs (Figure S6B), consistent with the higher degree of alloying or lattice shrinking.

2.2. Lattice Strain Sustainability under Electrocatalytic Reaction Conditions. *2.2.1. Correlation with the Activity.* Cyclic voltammetry (CV) curves and rotating disk electrode (RDE) data of Pt_nCu_{100-n}/C DNWs and SNWs with different compositions (Figure S8) provided an accelerated durability test (ADT) for the assessment. The mass and specific activities (MA and SA) are plotted against the compositions, along with the lattice constants, obtained from the corresponding characteristics (Figure 3A,C, Figures S9 and S10, and Tables S1−S6). The as-synthesized Pt contents in the catalysts (not the actual ones) after 50 cycles are shown in Figure 3A,C, and the corresponding actual Pt compositions are shown in Tables S1−S4. When it comes to samples with the same morphology with different compositions, the increase of MA and SA scales with the decrease of lattice constants when fresh (actual) Pt > 20 at. % (55 at. %). However, the MA and SA decrease with the lattice constant drop when as-synthesized (actual) Pt <20 at. % (55 at. %). It shows that both the ligand composition and lattice constant play a key role in the performance. The lattice constants of DNWs are smaller than those of SNWs at the same given Pt content (Figure 2D), suggestive of DNWs with a relatively higher compressive lattice strain. Compared with Figure 3A,C, we find that the MA and SA of DNWs are higher than those of SNWs at the same given positions, which means that the lattice strain plays a dominant

https://doi.org/10.1021/acscatal.4c00451
ACS Catal. 2024, 14, 4709−4718

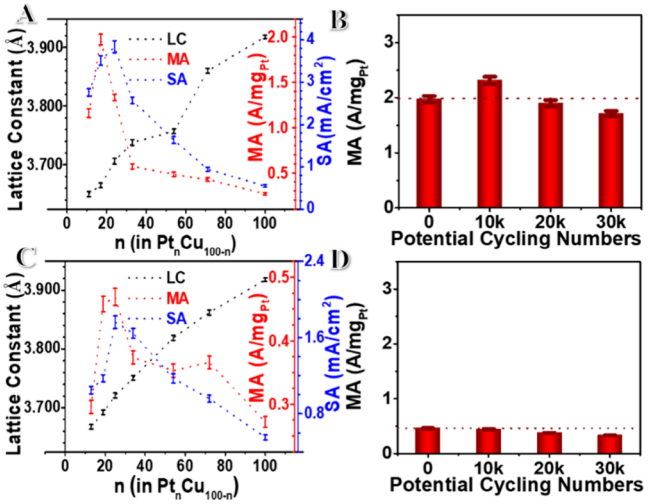

Figure 3. (A, C) Lattice constant, SA and MA vs Pt composition in Pt_nCu_{100-n}/C DNWs (A) and Pt_nCu_{100-n}/C SNWs (C), respectively. (B, D) The corresponding plots MA of $Pt_{17}Cu_{83}$/C DNWs (B) and $Pt_{18}Cu_{82}$/C SNWs (D) vs cycle numbers during ADT.

role as do the ligand compositions. Figure 2D shows that the lattice constants of DNWs are smaller than those of SNWs at the same given Pt content, suggestive of DNWs with relatively higher compressive strain. The conclusion is the same for both the fresh component and the actual component after 50 cycles (Figure S10 and Tables S2 and S4). Thus, the lattice compressive strain correlates with the activity enhancement.

We further compared the durability of DNWs and SNWs. The ADT data for the electrocatalytic durability of $Pt_{17}Cu_{83}$/C DNWs obtained from RDE curves recorded for 30,000 cycles is selectively shown in Figure S11A. Similar tests are shown in Figure S11B for $Pt_{18}Cu_{82}$/C SNWs. The MAs of Pt_nCu_{100-n}/C DNWs and SNWs during ADT are shown in Figure 3B and D at 0.90 V, respectively. By comparing the percentages of the activity decreases, the durability performance of $Pt_{17}Cu_{83}$/C DNWs (69%) is better than that of $Pt_{18}Cu_{82}$/C SNWs (53%) after 30,000 cycles based on ECSA data. As shown by the MA values of DNWs and SNWs in Figure 3B and D, respectively, the MA of DNWs increases from 100% (1.97 A/mg$_{Pt}$) to 117% (2.31 A/mg$_{Pt}$) at 10,000 cycles and then decreases gradually to 87% (1.71 A/mg$_{Pt}$) after 30,000 cycles at 0.90 V, with a total loss of 13% in MA. For the SNWs, the MA is shown to decrease by ∼28% of the initial value (0.458 A/mg$_{Pt}$) after 30,000 cycles at 0.90 V, respectively. Note that the corresponding performance extracted at 0.90 V was widely used by other reported literature. DNWs exhibit a high mass activity (2.31 A/mg$_{Pt}$ @0.90 V_{RHE}@10,000 cycles), to our knowledge, which is the best carbon-supported PtCu catalysts reported for ORR.[9] DNWs exhibit a five-times higher mass activity at 10,000 cycles than that of the best performance of SNWs, which is 9 and 14 times higher than Pt NWs and commercial Pt NPs, respectively.

To better understand the role of lattice strains in the high durability, the changes in lattice strains and surface sites for $Pt_{17}Cu_{83}$/C DNWs and $Pt_{18}Cu_{82}$/C SNWs are also compared. As suggested separately by XRD characteristic peaks and HRTEM characteristic features (Figures S12−S15 and Tables S5 and S8), there is only a subtle difference in crystal facets between DNWs and SNWs. The overall and surface compositions of the catalysts were measured before and after different stages of ADT using ICP and XPS (Figure S16A,B and Tables S9 and S10). As shown by TEM/EDS mapping and the line scan profile for the samples after 50 cycles of activation (Figure S17), both DNWs and SNWs exhibit a subtle inhomogeneity of the Pt and Cu distribution in comparison with those before activation (Figure 1 and Figure S17), which is consistent with the XRD data showing a partial compositional segregation in the dealloying process (Figure S18). Both $Pt_{17}Cu_{83}$/C DNWs and $Pt_{18}Cu_{82}$/C SNWs are shown to reach more than 65% Pt after the rapid leaching of Cu in the initial 500 cycles, which is followed by a gradual change to ∼75% Pt after 30,000 cycles, whose results abstracted from ICP. The Cu content of $Pt_{17}Cu_{83}$/C DNWs is higher than that of $Pt_{18}Cu_{82}$/C SNWs from 15,000 to 30,000 cycles. The XPS data show a similar change in terms of the relative surface composition (Figure S16B), which is slightly higher than the ICP-determined composition. An earlier work demonstrated that the adsorption on rough surfaces, including point defects, dislocations, vacancies, step terrace, and grain boundaries, exhibit a higher diffusion energy barrier than those of smooth ones.[35] From the perspective of metal atom coordination of the NW catalyst, the atomic diffusion coefficient is lower for DNWs with rough surfaces than SNWs. The results provided the first set of evidence supporting the assessment.

As shown by the lattice constant versus potential cycling for $Pt_{17}Cu_{83}$/C DNWs and $Pt_{18}Cu_{82}$/C SNWs in Figure 4A (Figure S16), the change in lattice constants is similar to the change in compositions before 500 cycles. Interestingly, the lattice constant shows a slow fluctuation pattern after 500 cycles for both types of NWs, suggestive of the dynamic change of the distance of the crystal cell and a realloying operation. Figure 4B shows a schematic of the DNWs and SNWs with different degrees of lattice strain. There is a consistently higher degree of compressive strain (∼1.8%) for DNWs in comparison with that of SNWs under the same given composition, especially in the realloying process (∼1.9%) when the ratio of Pt is higher than 60% (Table S12 and Figure 4C). The fact that there is a higher composition stability for DNWs than for SNWs at the same cycling numbers in ADT means that it is linked to the higher compressive strain (∼2.1%) (Table S13). Both of them are higher than the initial difference of lattice strain between SNWs and DNWs (∼1.6%). This assessment is also supported by the structural comparison of HE-XRD in terms of the increased alloying degree of the NWs after 10,000 ADT compared to that of the as-synthesized NWs (Figure S19). The lattice constant for DNWs remains smaller than that of SNWs throughout the cycles under the same given compositions (Figure 4D). There are different degrees of lattice compression for the two types of NW morphologies even at the same composition. In comparison with SNWs, DNWs are shown to maintain a higher degree of lattice compression due to a more effective realloying. Based on the overall trends of the lattice strain under the same potential cycling numbers (PCN) and the same given compositions for DNWs and SNWs (Tables S12 and S13), the higher lattice strain combined with the realloying operation plays a role in resisting the leaching of components and the decay of lattice constants.

A relatively higher Cu at. % was detected on the surface of DNWs than that of SNWs after the ADT. This finding is further assessed by the binding energies determined from XPS spectra at the different cycle numbers in ADT, which is shown to increase sharply from 0 to 10,000 cycles for DNWs,

https://doi.org/10.1021/acscatal.4c00451
ACS Catal. 2024, 14, 4709−4718

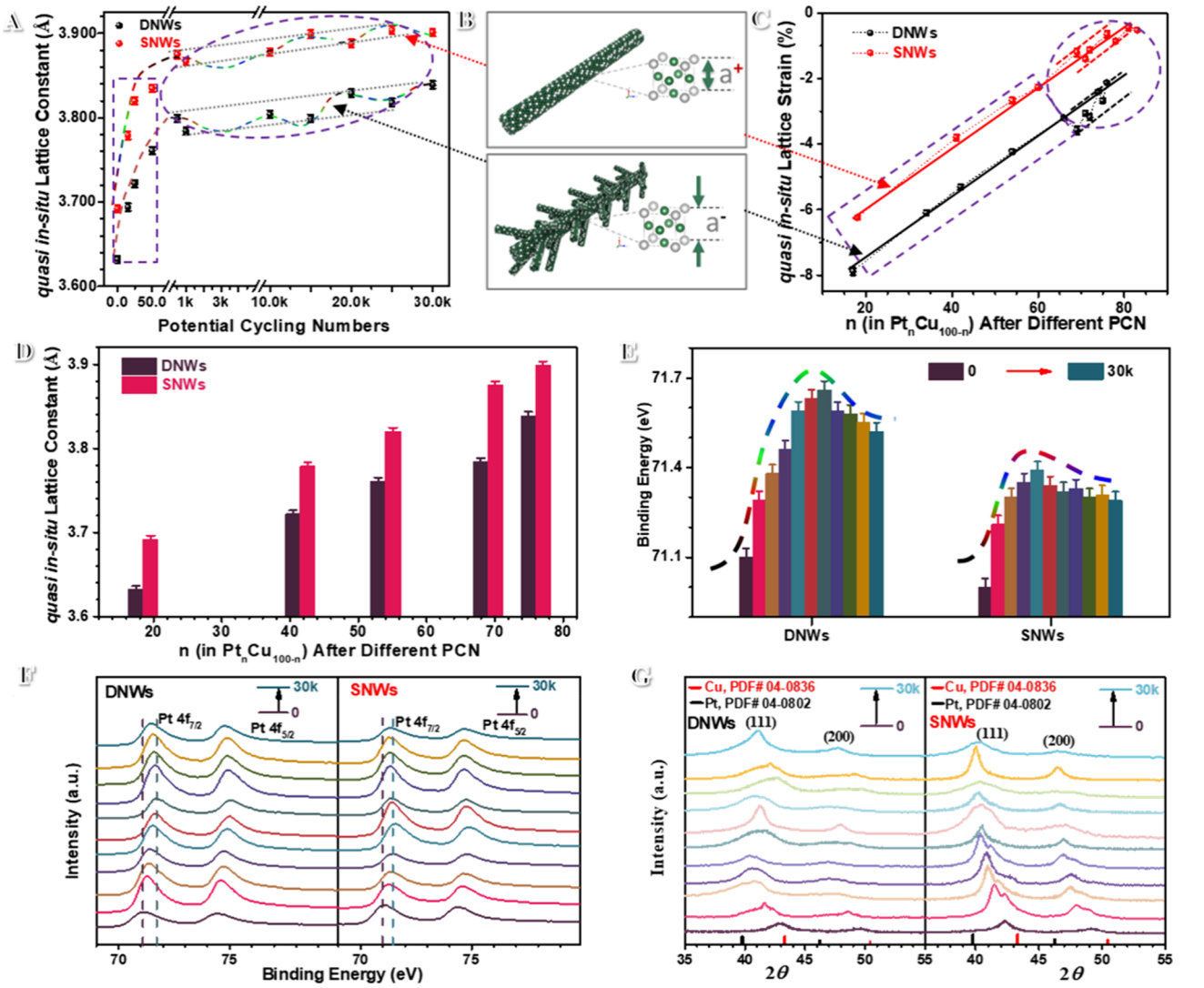

Figure 4. (A) Plots of lattice constant vs ADT potential cycling numbers (PCNs) for $Pt_{18}Cu_{82}$/C SNWs and $Pt_{17}Cu_{83}$/C DNWs. (B) Schematic diagram of DNWs and SNWs with different lattice compression. (C) Comparison of the changes of the compressive lattice strain between DNWs and SNWs throughout ADT. (D) Bar chart comparing the lattice constants between DNWs and SNWs under the same given compositions. (E, F) XPS spectra of Pt $4f_{7/2}$ for $Pt_{18}Cu_{82}$/C SNW and $Pt_{17}Cu_{83}$/C DNW samples from the ADT. (G) XRD patterns in the indicated 2θ range (from Figure S18) for the DNW and SNW samples from the ADT. The corresponding numbers of potential cycles in the ADT are 0, 15, 25, 50, 500, 1000, 5000, 10,000, 15,000, 20,000, and 30,000, respectively. Note that the lattice strain is given with respect to that of the pure Pt nanowires due to the main active element.

followed by a gradual decrease to some degree until to 30,000 cycles (Figure 4E,F and Figures S20 and 21). A similar trend is observed for SNWs but with a smaller amplitude. It is evident that there is a higher binding energy for DNWs than SNWs. An earlier observation of a negative shift in Pt 4f peak was attributed to a change of the electronic structure of Pt upon alloying with base metal, causing a downshift in the d-band center of Pt due to compressive strain.[9,15,18,34] Based on the electronegativity of Pt (2.28) and Cu (1.90), a decrease in binding energy is expected for Pt due to a partial charge transfer from Cu to Pt. Herein, for Figure 4F, as Cu content is largely decreased, there is a less partial charge transfer, resulting in an increase in the binding energy of Pt from initial to 10,000 cycles. The largely increased binding energy of Pt reflects Cu dealloying on the surface; after that, the obviously decreased binding energy suggests the possibility of realloying for the catalysts themselves, due to a very slight change of the concentration and composition for Cu and Pt in the electrolyte solution from 10,000 to 30,000 (Table S11). There is no indication of reaching constant binding energy like the Pt shell, supporting the occurrence of NWs realloying before 30,000 cycles, although the Pt-shell structure may eventually be formed after 30,000 cycles due to thermodynamic stability. As shown in Figure 4G, both $Pt_{17}Cu_{83}$/C DNWs and $Pt_{18}Cu_{82}$/C SNWs show subtle changes in the nanophase after the initial quick dealloying of Cu in the 50 to 500 cycles of the ADT. It is the dealloying that leads to the formation of fcc alloy phases with two different bimetallic compositions. However, a single-fcc alloy phase structure becomes evident after about 1000 cycles. The transformation to a single-fcc alloy phase reflects the operation of the subsequent and slow realloying process. In ADT, reallocation is more effective for DNWs to sustain the lattice compressive strain, which explains the enhanced durability and activity (Figure 3).

https://doi.org/10.1021/acscatal.4c00451
ACS Catal. 2024, 14, 4709−4718

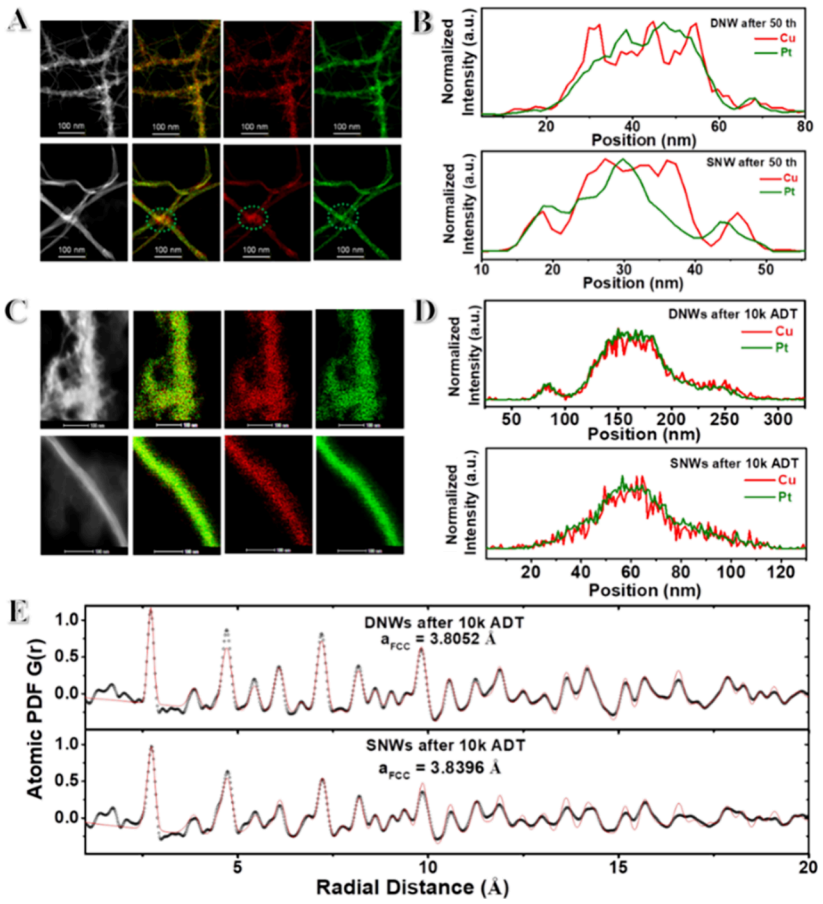

Figure 5. (A) HAADF-STEM and the corresponding EDS images of Cu (red) and Pt (green) of $Pt_{17}Cu_{83}$/C DNWs and $Pt_{18}Cu_{82}$/C SNWs after 50 ADT. (B) Line scan profiles for DNWs and SNWs after 50 ADT obtained from A (the line scan paths; see Figure S17). (C) HAADF-STEM and the corresponding EDS overlap images and EDS elemental mapping images of Cu (red) and Pt (green) of $Pt_{17}Cu_{83}$/C DNWs and $Pt_{18}Cu_{82}$/C SNWs after 10,000 ADT. (D) Line scan profiles of HAADF-STEM for $Pt_{17}Cu_{83}$/C DNWs and $Pt_{18}Cu_{82}$/C SNWs after 10,000 ADT (the line scan paths, see Figures S24 and S25). (E) Experimental PDF-fit and fcc-model fit to atomic PDFs for $Pt_{17}Cu_{83}$/C DNWs and $Pt_{18}Cu_{82}$/C SNWs after 10,000 ADT. The "fcc" lattice parameters are shown in it, which were refined by the analysis.

The apparent dealloying/realloying kinetics of the lattice constants and compositions were also extracted from XRD, and ICP and XPS were fitted by the first-order reaction model. The average rate constant (k) for the composition and lattice constant changes is smaller for DNWs than that for SNWs (Figure 4B and Figure S16 inset). The change in leaching ratio (k) for the lattice constant and composition of DNWs is smaller than that for SNWs under the same given composition (Figure S22). This indicates that the high lattice strain retards the metal leaching ratio as well as the change of the crystal cell distance. The migration or diffusion is confidently confirmed by TEM characterization, showing the appearance of internal voids for both DNWs and SNWs after ADT (Figure S14). The long-term migration of Cu atoms from inside to outside, displacing the leached atoms located in the outer crystal cell, causes both the dealloying and the realloying operation (details in Figure S23).

Upon increasing the cycling number, the relative leaching of Cu decreases while realloying slowly picks up, which is accompanied by the evolution of the microstructures/atomic rearrangement (refer to Figure S23 for the schematic diagram, Figures S15 and S18). This is supported by the observation of a relatively uniform composition across the random alloy structure for both DNWs and SNWs after 10,000 ADT (Figure 5 in the next section). It is the difference in lattice strain between DNWs and SNWs that led to the different kinetics during ADT.

2.3. Correlation with Durability. In comparison with the EDS mapping and line scan data after 50 cycles of activation (Figure 5A,B), there is an indication of inhomogeneity for the composition distribution on the surface due to the too fast dealloying in the initial procedure, which is consistent with segregation structures (two fcc-alloyed phases with different bimetallic compositions) inferred from the XRD pattern from 50 to 500 cycles (Figure S18). The different long-range correlation characteristics, as shown in the HE-XRD/PDF (Figure 2B), reflect different degrees of alloying in the NWs. DNWs exhibit phase segregation in the first 50 cycles of ADT (Figure 5) and are thus indicative of an initial leaching stage due to dealloying from the NWs, leading to the formation of mixed alloy phases. As shown in Figure 5C and D by the EDS and the corresponding line scan profiles of $Pt_{17}Cu_{83}$/C DNWs and $Pt_{18}Cu_{82}$/C SNWs, respectively, both catalysts after 10,000 cycles exhibit uniform Pt and Cu distributions along and across the DNWs and SNWs. There are no apparent morphological changes for both DNWs and SNWs (Figures S24 and S25).

The phase structures of the as-synthesized NWs were compared with those after ADT based on HE-XRD/PDF characterizations, showing an increased degree of close-packing alloying of NWs in the realloying process. This is evidenced by

https://doi.org/10.1021/acscatal.4c00451
ACS Catal. 2024, 14, 4709−4718

the increased uniformity of the elemental distribution based on EDS and the increased PDF signal intensity at larger radial distances after ADT (Figure S19). As shown in Figure 5E from experimental PDF-fit and fcc-model fit to atomic PDFs for $Pt_{17}Cu_{83}$/C DNWs and $Pt_{18}Cu_{82}$/C SNWs after 10,000 cycles in ADT, a smaller lattice constant is evident for DNWs than for SNWs. There is clearly a higher compressive strain for DNWs than for SNWs due to the same composition. The higher degree of the compressive lattice strain of DNWs than SNWs exhibits a stronger ability to resist the decrease of the compressive lattice strain during ADT, leading thus to a stronger tendency toward a single-phase structure, verified by both in-house XRD and HE-XRD/PDF data (Figure 5 and Figures S18 and S19). After 10,000 cycles (Figure 5), the realloying process forms a Pt-rich alloy, showing an increased uniformity in terms of composition distribution especially for DNWs, which enhanced the durability. This is consistent with the HE-XRD results for the enhanced alloying structure of both NWs, especially for DNWs, without any indication of the core−shell type of distribution after 10,000 cycles (Figures 2 and 5 and Figure S19). It is the effective dealloying−realloying operation (schematic diagram; see Figure S23) combined with a higher compressive strain that is responsible for the enhanced activity and durability for DNWs. After 30,000 cycles, DNWs still showed more dendritic morphology than SNWs (Figure S14B,E).

2.4. Theoretical Assessment. To further assess the morphological impact on the lattice strains (Figure S26) and the catalytic activity, DFT calculations based on two slab models are built to simulate the bimetallic PtCu alloy NWs in relation to the dendritic and smooth structural features (Figure 6A). The dendritic feature is reflected by the surface-anchored Pt atoms, which show relatively high levels of unsaturated coordination bonds as well as surface lattice strain due to the enhanced surface energy in comparison with the underlying atomic layers. In contrast, the smooth feature is reflected by the (111) surface-terminated slab model. The surface lattice strain of DNW is generated after the geometric optimization, which indicates a higher degree of compressive strain of DNW in comparison to that of SNW. The results also demonstrate that the degree of the relative surface compressive strain increases with the decreased coverage of surface atoms on DNW (Figure 6B). We note here that the relative surface strain is defined as the lattice parameter difference between the surface atoms of the DNW model and the underneath atoms, which is different from the overall lattice strain in the NW. There is a correlation between the coordination environments of atoms, which depends on the morphology of the NW, and the compressive strain in the alloy.

The structure−activity correlation for the electrochemical performance is also assessed based on the DNW and SNW models (Figure 6C). A computational hydrogen electrode (CHE)[36] is used to reflect the electrochemical potential in the theoretical calculation. At $U = 0$, the free energy profiles of two models show similar features with four downhill steps, demonstrating the exothermic nature of each elementary step. Stronger bindings are exhibited on the DNW model compared to the SNW model. This is consistent with the high-coordination unsaturated atoms and the resulting compressive strain on the surface of the DNW model. At $U = 0.9$ V, a potential close to the experimental onset potential for the ORR, the free energy profiles provided useful information. The free energy changes (ΔG) for the first two steps remain

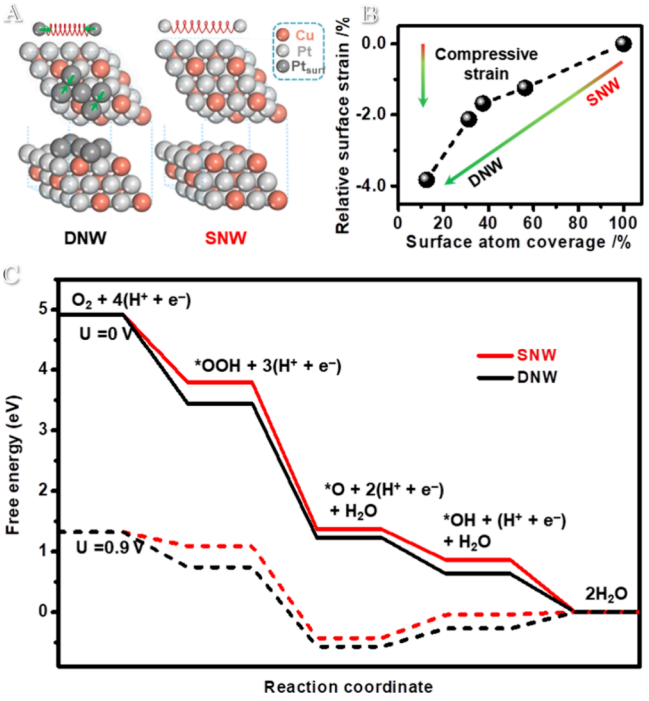

Figure 6. (A) Schematic illustration of the morphologies and lattice strains for DNW and SNW. (B) DFT models for DNW and SNW, including the relative compressive strain of surface atoms. (C) Plot of the relative surface strain to underlying bulk layers and the surface atom coverage in the surface layer of the DNW model. Negative values of the relative surface strain represent the compressive strain. (D) The free energy profiles are based on DNW and SNW models at $U = 0$ and 0.9 V vs RHE.

negative. However, the ΔG values for the last two steps become positive, i.e., endothermic. The rate-determining step (RDS) at $U = 0.9$ V for both DNW and SNW models is the protonation of the *O intermediate with positive ΔG values at 0.30 and 0.39 eV, respectively. The result suggests that the completion of ORR on DNW has a higher favorability than on SNW. This finding serves as an important clue for assessing the experimentally observed ORR activity over DNWs being higher than that of SNWs in terms of morphological impact on the lattice strain.

3. CONCLUSIONS

In conclusion, the dendritic PtCu alloy nanowires are shown to exhibit the best ORR performance among the reported PtCu/C catalysts. The increased activity and durability of the low-Pt-content DNW catalysts are shown to originate from a strong morphology-regulated compressive strain in correlation with the composition and structure of Pt-based alloy NWs during the dealloying−realloying processes. The compressed lattice of DNWs plays a crucial role in enabling a stable Pt-rich alloy structure across the entire NWs. Due to the effective realloying, the dendritic morphology with an initially higher lattice compressive strain enables the the NWs with the capability to maintain the relative higher compressively strained lattice and the single-phase fcc structure, which is remarkable considering the low-Pt content (<20%) in the as-prepared alloy NWs. The DNWs exhibit an ∼1.8% higher compressive strain under the same compositions, and ∼2.1% higher compressive strain in the same cycling time compared to SNWs throughout the electrocatalysis process. Both are

https://doi.org/10.1021/acscatal.4c00451
ACS Catal. 2024, 14, 4709−4718

higher than the initial strain difference between SNWs and DNWs (~1.6%). This finding is to our knowledge the first example demonstrating the role of the morphology-tunable compressive strain in regulating the composition and phase structure of nanowires and consequently boosting the activity and durability. The insight into the morphology−composition−activity relationships in terms of the lattice strain will have implications for the design of active and stable catalysts in fuel cell applications.

■ ASSOCIATED CONTENT

Data Availability Statement

The data sets generated and/or analyzed in the current study are available from the corresponding authors upon reasonable request and are also included with the manuscript as Supporting Information.

Supporting Information

The Supporting Information is available free of charge at https://pubs.acs.org/doi/10.1021/acscatal.4c00451.

Methods with experimental and measurement details; characterization data including TEM images, STEM images, SEM images, XRD patterns, HE-XED/PDF data, XPS data, ICP data, CV curves, RDE curves, and ADT data; and mass activity data, specific activity data, ECSA data, lattice constant data, and lattice strain data (PDF)

■ AUTHOR INFORMATION

Corresponding Authors

Chuan-Jian Zhong − *Department of Chemistry, State University of New York at Binghamton, Binghamton, New York 13902, United States;* orcid.org/0000-0003-0746-250X; Email: cjzhong@binghamton.edu

Shuang-Quan Zang − *Henan Key Laboratory of Crystalline Molecular Functional Materials, Green Catalysis Center, College of Chemistry, Zhengzhou University, Zhengzhou 450001, China;* orcid.org/0000-0002-6728-0559; Email: zangsqzg@zzu.edu.cn

Li Tao − *State Key Laboratory of Chem/Bio-Sensing and Chemometrics, Provincial Hunan Key Laboratory for Graphene Materials and Devices, College of Chemistry and Chemical Engineering, the National Supercomputer Centers in Changsha, Hunan University, Changsha 410082, China;* Email: taoli@hnu.edu.cn

Shuangyin Wang − *State Key Laboratory of Chem/Bio-Sensing and Chemometrics, Provincial Hunan Key Laboratory for Graphene Materials and Devices, College of Chemistry and Chemical Engineering, the National Supercomputer Centers in Changsha, Hunan University, Changsha 410082, China;* orcid.org/0000-0001-7185-9857; Email: shuangyinwang@hnu.edu.cn

Authors

Zhijie Kong − *Henan Key Laboratory of Crystalline Molecular Functional Materials, Green Catalysis Center, College of Chemistry, Zhengzhou University, Zhengzhou 450001, China; Department of Chemistry, State University of New York at Binghamton, Binghamton, New York 13902, United States; State Key Laboratory of Chem/Bio-Sensing and Chemometrics, Provincial Hunan Key Laboratory for Graphene Materials and Devices, College of Chemistry and Chemical Engineering, the National Supercomputer Centers in Changsha, Hunan University, Changsha 410082, China*

Zhi-Peng Wu − *Department of Chemistry, State University of New York at Binghamton, Binghamton, New York 13902, United States; Henan Key Laboratory of Crystalline Molecular Functional Materials, Green Catalysis Center, College of Chemistry, Zhengzhou University, Zhengzhou 450001, China;* orcid.org/0000-0002-5422-1349

Yazan Maswadeh − *Department of Physics, Central Michigan University, Mount Pleasant, Michigan 48859, United States*

Gang Yu − *State Key Laboratory of Chem/Bio-Sensing and Chemometrics, Provincial Hunan Key Laboratory for Graphene Materials and Devices, College of Chemistry and Chemical Engineering, the National Supercomputer Centers in Changsha, Hunan University, Changsha 410082, China*

Jorge A. Vargas − *Department of Physics, Central Michigan University, Mount Pleasant, Michigan 48859, United States;* orcid.org/0000-0002-9651-8183

Dominic Caracciolo − *Department of Chemistry, State University of New York at Binghamton, Binghamton, New York 13902, United States*

Valeri Petkov − *Department of Physics, Central Michigan University, Mount Pleasant, Michigan 48859, United States;* orcid.org/0000-0002-6392-7589

Complete contact information is available at: https://pubs.acs.org/10.1021/acscatal.4c00451

Author Contributions

Z.K. and C.-J.Z. proposed the original idea. Z.K. performed most experiments and carried out the data analysis. Z.K. and C.-J.Z. wrote and revised the manuscript. Z.-P.W. carried out the DFT calculations and revised the manuscript. Y.M., Z.K., Z.-P.W., J.A.V., and V.P. carried out in situ synchrotron HE-XRD experiments. D.C. and L.T. carried out partial performance and in-house XRD tests. S.-Q.Z., G.Y., and S.W. revised the manuscript. C.-J.Z. supervised the entire research project, conceived and designed the experiments, coordinated the research collaborations, and wrote and revised the manuscript. All participated in the discussions and revisions of the manuscript.

Notes

The authors declare no competing financial interest.

■ ACKNOWLEDGMENTS

This work was supported by the US National Science Foundation (CHE 2102482 and 1566283), the National Key R&D Program of China (SQ2020YFA070100), and in part the NNSF of China (22109042, 51271074), China Postdoctoral Science Foundation (2021M701142), and the US Department of Energy-Basic Energy Science (DE-SC0006877). The experiments of synchrotron X-ray diffraction were performed at Beamline 11-ID-C of the Advanced Photon Source, a U.S. Department of Energy (DOE) Office of Science User Facility, which is operated for the DOE Office of Science by Argonne National Laboratory under Contract No. DE-AC02-06CH11357.

■ REFERENCES

(1) Wu, Z. P.; Caracciolo, D. T.; Maswadeh, Y.; Wen, J.; Kong, Z.; Shan, S.; Vargas, J. A.; Yan, S.; Hopkins, E.; Park, K.; Sharma, A.; Ren, Y.; Petkov, V.; Wang, L.; Zhong, C. J. Alloying-realloying enabled high

durability for Pt-Pd-3d-transition metal nanoparticle fuel cell catalysts. *Nat. Commun.* **2021**, *12* (1), 859.
(2) Zhong, C. J.; Luo, J.; Njoki, P. N.; Mott, D.; Wanjala, B.; Loukrakpam, R.; Lim, S.; Wang, L.; Fang, B.; Xu, Z. Fuel cell technology: nano-engineered multimetallic catalysts. *Energy Environ. Sci.* **2008**, *1*, 454−466.
(3) Chen, S.; Su, H. Y.; Wang, Y. C.; Wu, W. L.; Zeng, J. Size-controlled synthesis of platinum-copper hierarchical trigonal bipyramid nanoframes. *Angew. Chem., Int. Ed.* **2015**, *54* (1), 108−113.
(4) Zhang, Z.; Luo, Z.; Chen, B.; Wei, C.; Zhao, J.; Chen, J.; Zhang, X.; Lai, Z.; Fan, Z.; Tan, C.; Zhao, M.; Lu, Q.; Li, B.; Zong, Y.; Yan, C.; Wang, G.; Xu, Z. J.; Zhang, H. One-pot synthesis of highly anisotropic five-fold-twinned PtCu nanoframes used as a bifunctional electrocatalyst for oxygen reduction and methanol oxidation. *Adv. Mater.* **2016**, *28*, 8712.
(5) Ao, X.; Zhang, W.; Zhao, B.; Ding, Y.; Nam, G.; Soule, L.; Abdelhafiz, A.; Wang, C.; Liu, M. Atomically dispersed single iron sites for promoting Pt and Pt_3Co fuel cell catalysts: performance and durability improvements. *Energy Environ. Sci.* **2020**, *13*, 3032−3040.
(6) Wu, Z. P.; Shan, S.; Zang, S. Q.; Zhong, C. J. Dynamic core-shell and alloy structures of multimetallic nanomaterials and their catalytic synergies. *Acc. Chem. Res.* **2020**, *53*, 2913−2924.
(7) Chang, F. F.; Shan, S. Y.; Petkov, V.; Skeete, Z.; Lu, A. L.; Ravid, J.; Wu, J. F.; Luo, J.; Yu, G.; Ren, Y.; Zhong, C. J. Composition tunability and (111)-dominant facets of ultrathin platinum-gold alloy nanowires toward enhanced electrocatalysis. *J. Am. Chem. Soc.* **2016**, *138* (37), 12166−12175.
(8) Luo, M.; Sun, Y.; Zhang, X.; Qin, Y.; Li, M.; Li, Y.; Li, C.; Yang, Y.; Wang, L.; Gao, P.; Lu, G.; Guo, S. Stable high-index faceted pt skin on zigzag-like PtFe nanowires enhances oxygen reduction catalysis. *Adv. Mater.* **2018**, *30*, 1705515.
(9) Guo, N.; Xue, H.; Bao, A.; Wang, Z.; Sun, J.; Song, T.; Ge, X.; Zhang, W.; Huang, K.; He, F.; Wang, Q. Achieving superior electrocatalytic performance by surface copper vacancy defects during electrochemical etching process. *Angew. Chem., Int. Ed.* **2020**, *59*, 13778−13784.
(10) Yang, J.; Chen, X.; Yang, X.; Ying, J. Y. Stabilization and compressive strain effect of AuCu core on Pt shell for oxygen reduction reaction. *Energy Environ. Sci.* **2012**, *5*, 8976.
(11) Wang, D. L.; Yu, Y. C.; Xin, H. L. L.; Hovden, R.; Ercius, P.; Mundy, J. A.; Chen, H.; Richard, J. H.; Muller, D. A.; DiSalvo, F. J.; Abruna, H. D. Tuning Oxygen Reduction Reaction Activity via Controllable dealloying: A Model Study of Ordered Cu3Pt/C Intermetallic Nanocatalysts. *Nano Lett.* **2012**, *12* (10), 5230−5238.
(12) Greeley, J.; Norskov, J. K. Electrochemical dissolution of surface alloys in acids: Thermodynamic trends from first-principles calculations. *Electrochim. Acta* **2007**, *52* (19), 5829−5836.
(13) Stephens, I. E. L.; Bondarenko, A. S.; Gronbjerg, U.; Rossmeisl, J.; Chorkendorff, I. Understanding the electrocatalysis of oxygen reduction on platinum and its alloys. *Energy Environ. Sci.* **2012**, *5*, 6744−6762.
(14) Jia, Q. Y.; Liang, W. T.; Bates, M. K.; Mani, P.; Lee, W.; Mukerjee, S. Activity Descriptor Identification for Oxygen Reduction on Platinum-Based Bimetallic Nanoparticles: In Situ Observation of the Linear Composition-Strain-Activity Relationship. *ACS Nano* **2015**, *9* (1), 387−400.
(15) Petkov, V.; Maswadeh, Y.; Vargas, J. A.; Shan, S. Y.; Kareem, H.; Wu, Z. P.; Luo, J.; Zhong, C. J.; Shastri, S.; Kenesei, P. Deviations from Vegard's law and evolution of the electrocatalytic activity and stability of Pt-based nanoalloys inside fuel cells by in operando X-ray spectroscopy and total scattering. *Nanoscale* **2019**, *11* (12), 5512−5525.
(16) Srivastava, R.; Mani, P.; Hahn, N.; Strasser, P. Efficient oxygen reduction fuel cell electrocatalysis on voltammetrically dealloyed Pt-Cu-Co nanoparticles. *Angew. Chem., Int. Ed.* **2007**, *46* (47), 8988−8991.
(17) Wang, D. L.; Yu, Y. C.; Zhu, J.; Liu, S. F.; Muller, D. A.; Abruna, H. D. Morphology and Activity Tuning of Cu_3Pt/C Ordered Intermetallic Nanoparticles by Selective Electrochemical dealloying. *Nano Lett.* **2015**, *15* (2), 1343−1348.
(18) Kong, Z. J.; Maswadeh, Y.; Vargas, J. A.; Shan, S. Y.; Wu, Z. P.; Kareem, H.; Leff, A. C.; Tran, D. T.; Chang, F. F.; Yan, S.; Nam, S.; Zhao, X. F.; Lee, J. M.; Luo, J.; Shastri, S.; Yu, G.; Petkov, V.; Zhong, C. J. Origin of high activity and durability of twisty nanowire alloy catalysts under oxygen reduction and fuel cell operating conditions. *J. Am. Chem. Soc.* **2020**, *142* (3), 1287−1299.
(19) Li, M.; Zhao, Z.; Cheng, T.; Fortunelli, A.; Chen, C. Y.; Yu, R.; Zhang, Q.; Gu, L.; Merinov, B. V.; Lin, Z.; Zhu, E.; Yu, T.; Jia, Q.; Guo, J.; Zhang, L.; Goddard, W. A., 3rd; Huang, Y.; Duan, X. Ultrafine jagged platinum nanowires enable ultrahigh mass activity for the oxygen reduction reaction. *Science* **2016**, *354*, 1414.
(20) Strasser, P.; Koh, S.; Anniyev, T.; Greeley, J.; More, K.; Yu, C. F.; Liu, Z. C.; Kaya, S.; Nordlund, D.; Ogasawara, H.; Toney, M. F.; Nilsson, A. Lattice-strain control of the activity in dealloyed core-shell fuel cell catalysts. *Nat. Chem.* **2010**, *2* (6), 454−460.
(21) Cui, C. H.; Gan, L.; Heggen, M.; Rudi, S.; Strasser, P. Compositional segregation in shaped Pt alloy nanoparticles and their structural behaviour during electrocatalysis. *Nat. Mater.* **2013**, *12* (8), 765−771.
(22) Chen, C.; Kang, Y.; Huo, Z.; Zhu, Z.; Huang, W.; Xin, H. L.; Snyder, J. D.; Li, D.; Herron, J. A.; Mavrikakis, M.; Chi, M.; More, K. L.; Li, Y.; Markovic, N. M.; Somorjai, G. A.; Yang, P. D.; Stamenkovic, V. R. Highly crystalline multimetallic nanoframes with three-dimensional electrocatalytic surfaces. *Science* **2014**, *343*, 1339−1343.
(23) Moseley, P.; Curtin, W. A. Computational design of strain in core-shell nanoparticles for optimizing catalytic activity. *Nano Lett.* **2015**, *15* (6), 4089−4095.
(24) Chattot, R.; Asset, T.; Bordet, P.; Drnec, J.; Dubau, L.; Maillard, F. Beyond strain and ligand effects: Microstrain-induced enhancement of the oxygen reduction reaction kinetics on various PtNi/C nanostructures. *ACS Catal.* **2017**, *7* (1), 398−408.
(25) Shan, S.; Li, J.; Maswadeh, Y.; O'Brien, C.; Kareem, H.; Tran, D. T.; Lee, I. C.; Wu, Z. P.; Wang, S.; Yan, S.; Cronk, H.; Mott, D.; Yang, L.; Luo, J.; Petkov, V.; Zhong, C. J. Surface oxygenation of multicomponent nanoparticles toward active and stable oxidation catalysts. *Nat. Commun.* **2020**, *11* (1), 1−9.
(26) Lei, D.; Benson, J.; Magasinski, A.; Berdichevsky, G.; Yushin, G. Transformation of bulk alloys to oxide nanowires. *Science* **2017**, *355*, 267−270.
(27) Garnett, E.; Mai, L.; Yang, P. Introduction: 1D nanomaterials/nanowires. *Chem. Rev.* **2019**, *119*, 8955−8957.
(28) Glas, F. Strain in nanowires and nanowire heterostructures. *Semiconduct Semimet* **2015**, *93*, 79−123.
(29) Gan, L.; Yu, R.; Luo, J.; Cheng, Z.; Zhu, J. Lattice strain distributions in individual dealloyed Pt-Fe catalyst nanoparticles. *J. Phys. Chem. Lett.* **2012**, *3*, 934−938.
(30) Xia, Z.; Guo, S. Strain engineering of metal-based nanomaterials for energy electrocatalysis. *Chem. Soc. Rev.* **2019**, *48*, 3265−3278.
(31) Zhang, N.; Bu, L.; Guo, S.; Guo, J.; Huang, X. Screw thread-like platinum-copper nanowires bounded with high-index facets for efficient electrocatalysis. *Nano Lett.* **2016**, *16*, 5037−5043.
(32) Xia, B. Y.; Wu, H. B.; Yan, Y.; Lou, X. W.; Wang, X. Ultrathin and ultralong single-crystal platinum nanowire assemblies with highly stable electrocatalytic activity. *J. Am. Chem. Soc.* **2013**, *135* (25), 94809−485.
(33) Zhang, S.; Ma, Y.; Zhang, H.; Zhou, X.; Chen, X.; Qu, Y. Additive-Free, Robust H_2 Production from H_2O and DMF by Dehydrogenation Catalyzed by Cu/Cu_2O Formed In Situ. *Angew. Chem., Int. Ed.* **2017**, *56* (28), 8245−8249.
(34) Fang, D. H.; Wan, L.; Jiang, Q. K.; Zhang, H. J.; Tang, X. J.; Qin, X. P.; Shao, Z. G.; Wei, Z. D. Wavy PtCu alloy nanowire networks with abundant surface defects enhanced oxygen reduction reaction. *Nano Res.* **2019**, *12* (11), 2766−2773.
(35) Ranguelov, B.; Michailov, M. 18th International School on Condensed Matter Physics. *Challenges of Nanoscale Science: Theory, Materials, Applications* **2014**, *558*, No. 012004.

https://doi.org/10.1021/acscatal.4c00451
ACS Catal. 2024, 14, 4709−4718

(36) Nørskov, J. K.; Rossmeisl, J.; Logadottir, A.; Lindqvist, L.; Kitchin, J. R.; Bligaard, T.; Jónsson, H. Origin of the overpotential for oxygen reduction at a fuel-cell cathode. *Phys. Chem. B* **2004**, *108* (46), 17886−17892.

https://doi.org/10.1021/acscatal.4c00451
ACS Catal. 2024, 14, 4709−4718